

1 Asymmetric intraseasonal events in the stochastic skeleton
2 MJO model with seasonal cycle

3
4 Sulian Thual ⁽¹⁾, Andrew J. Majda ⁽¹⁾, and Samuel N. Stechmann ⁽²⁾

5 (1) Department of Mathematics, and Center for Atmosphere Ocean Science, Courant Institute of
6 Mathematical Sciences, New York University, 251 Mercer Street, New York, NY 10012 USA

7 (2) Department of Mathematics, and Department of Atmospheric and Oceanic Sciences, University
8 of Wisconsin - Madison, 480 Lincoln Drive, Madison, WI 53706 USA

9 Corresponding author:

10 Sulian Thual, 251 Mercer Street, New York, NY 10012 USA, *sulian.thual@gmail.com*

11 *Submitted to Climate Dynamics, April 2014*

12 **Abstract**

13 The stochastic skeleton model is a simplified model for the Madden-Julian oscil-
14 lation (MJO) and intraseasonal-planetary variability in general involving coupling of
15 planetary-scale dry dynamics, moisture, and a stochastic parametrization for the unre-
16 solved details of synoptic-scale activity. The model captures the fundamental features
17 of the MJO such as the intermittent growth and demise of MJO wave trains, the MJO
18 propagation speed, peculiar dispersion relation, quadrupole vortex structure, etc. We
19 analyze here the solutions of a stochastic skeleton model with an idealized seasonal
20 cycle, namely a background warm pool state of heating/moistening displacing merid-
21 ionally during the year. The present model considers both equatorial and off-equatorial

22 components of the envelope of synoptic scale convective activity, which allows for a
23 large diversity of meridionally symmetric and asymmetric intraseasonal events found
24 in nature. These include examples of symmetric events with MJO quadrupole vor-
25 tex structure, half-quadrupole events with off-equatorial convective heating structure,
26 as well as tilted events with convective heating structure oriented north-westward and
27 associated northward propagation that is reminiscent of the summer monsoon intrasea-
28 sonal oscillation. The model also reproduces qualitatively the meridional migration of
29 intraseasonal variability during the year, that approximatively follows the meridional
30 migration of the background warm pool.

31 **1 Introduction**

32 The dominant component of intraseasonal variability in the tropics is the 40 to 50 day intraseasonal
33 oscillation, often called the Madden-Julian oscillation (MJO) after its discoverers (Madden and
34 Julian, 1971; 1994). In the troposphere, the MJO is an equatorial planetary-scale wave, that is
35 most active over the Indian and western Pacific oceans and propagates eastward at a speed of
36 around 5 ms^{-1} . The planetary-scale circulation anomalies associated with the MJO significantly
37 affect monsoon development, intraseasonal predictability in midlatitudes, and the development of
38 El Niño events in the Pacific ocean, which is one of the most important components of seasonal
39 prediction.

40 One fundamental and not fully understood characteristic of the MJO and the intraseasonal
41 oscillation (ISO) in the tropics in general is its pronounced seasonality. The MJO signals migrate in
42 latitude during the year, approximatively following the migration of warm sea surface temperatures,
43 with for example a peak activity of zonal winds and precipitation located slightly south of the
44 equator in boreal winter and north of the equator in boreal summer (Salby and Hendon, 1994;
45 Zhang and Dong, 2004). The MJO is strongest during the boreal winter and spring seasons
46 where it appears as a predominantly eastward propagating system of convection along (or slightly
47 south of) the equator. Noteworthy the MJO signals in boreal winter are related to the onset and
48 breaks of the Australian monsoon (Wheeler and Hendon, 2004; Lau and Waliser, 2012 chapt 5).

49 In boreal summer, the ISO is of a different character: the dominant intraseasonal oscillation, of
50 period 30-60 days, shows a pronounced off-equatorial component that is associated in particular
51 with northward or north-eastward propagation of convection over the Indian ocean and the Asian
52 continent (Zhang, 2005; Kikuchi et al., 2011). This intraseasonal mode is sometimes referred to
53 as the summer monsoon ISO, or boreal summer ISO, in order to differentiate it from the boreal
54 winter MJO. Several studies interpret the northward propagation as resulting from the interaction
55 between the eastward propagation of convection at the equator (e.g. the northern gyre of equatorial
56 Rossby waves forced by equatorial convective heating) and the background mean state (Lau and
57 Peng, 1990; Wang and Xie, 1997; Lawrence and Webster, 2002), though there is also observational
58 and theoretical evidence that northward propagation can be independent (Webster, 1983; Wang
59 and Rui, 1990; Jiang et al., 2004; Annamalai and Sperber, 2005). The summer monsoon ISO
60 signals are strongly related to the onset and breaks of the South Asian and East Asian monsoon
61 (Lau and Waliser, 2012 chapt 2, 3).

62 In addition to such climatological features, the structure of individual intraseasonal events is
63 often unique. For example, both equatorial and off-equatorial convective heating coexist during
64 intraseasonal events with characteristics and intensity that differ from one event to another (Wang
65 and Rui, 1990; Jones et al., 2004; Masunaga, 2007), including during MJO events (Tung et al.,
66 2014a, b). Biello and Majda (2005, 2006) for example have analyzed in a multiscale model for
67 the MJO the differences in planetary-scale circulation induced by equatorial or off-equatorial con-
68 vective heating of synoptic-scale. Individual intraseasonal events also show unique refined vertical
69 structures as well as complex dynamic and convective features within their envelope. The MJO for
70 example shows front-to-rear vertical tilts, westerly wind bursts, etc within its envelope (Kikuchi
71 and Takayabu, 2004; Kiladis et al., 2005; Tian et al., 2006), while the summer monsoon ISO shows
72 dynamic and convective features of a different nature (Goswami et al., 2003; Straub and Kiladis,
73 2003)

74 Despite the primary importance of the MJO and the decades of research progress since its
75 original discovery, no theory for the MJO has yet been generally accepted. Simple theories provide
76 some useful insight on certain isolated aspects of the MJO, but they have been largely unsuccessful

77 in reproducing all of its fundamental features together (Zhang, 2005). Meanwhile, present-day
78 simulations by general circulation models (GCMs) typically have poor representations of it, despite
79 some recent improvements (Lin et al., 2006; Kim et al., 2009; Hung et al., 2013). A growing body
80 of evidence suggests that this poor performance of both theories and simulations in general is
81 due to the inadequate treatment of the organized structures of tropical convection (convectively-
82 coupled waves, cloud-clusters...), that are defined on a vast range of spatiotemporal scales (synoptic,
83 mesoscale...) and that generate the MJO as their planetary envelope (Hendon and Liebmann,
84 1994; Moncrieff et al., 2007). For example, in current GCMs and models in general computing
85 resources significantly limit spatial grids (to $\approx 10 - 100 km$), and therefore there are several
86 important small scale moist processes that are unresolved or parametrized according to various
87 recipes. Insight has been gained from the study of MJO-like waves in multcloud model simulations
88 and in superparametrization computer simulations, which appear to capture many of the observed
89 features of the MJO by accounting for coherent smaller-scale convective structures within the
90 MJO envelope (e.g. Grabowski and Moncrieff, 2004; Majda et al., 2007; Khouider et al., 2011;
91 Ajayamohan et al., 2013). Suitable stochastic parametrizations also appear to be good candidates
92 to account for irregular and intermittent organized small scale moist processes while remaining
93 computationally efficient (Majda et al., 2008; Khouider et al., 2010; Stechmann and Neelin, 2011;
94 Frenkel et al., 2012; Deng et al., 2014). As another example, the role of synoptic scale waves in
95 producing key features of the MJO’s planetary scale envelope has been elucidated in multiscale
96 asymptotic models (Majda and Biello, 2004; Biello and Majda, 2005, 2006; Majda and Stechmann,
97 2009a; Stechmann et al., 2013).

98 While theory and simulation of the MJO remain difficult challenges, they are guided by some
99 generally accepted, fundamental features of the MJO on intraseasonal-planetary scales that have
100 been identified relatively clearly in observations (Hendon and Salby, 1994; Wheeler and Kiladis,
101 1999; Zhang, 2005). These features are referred to here as the MJO’s “skeleton” features:

- 102 I. A slow eastward phase speed of roughly $5 ms^{-1}$,
- 103 II. A peculiar dispersion relation with $d\omega/dk \approx 0$, and
- 104 III. A horizontal quadrupole structure.

105 Recently, Majda and Stechmann (2009b) introduced a minimal dynamical model, the skeleton
106 model, that captures the MJO's intraseasonal features (I-III) together for the first time in a simple
107 model. The model is a coupled nonlinear oscillator model for the MJO skeleton features as well
108 as tropical intraseasonal variability in general. In particular, there is no instability mechanism
109 at planetary scale, and the interaction with sub-planetary convective processes discussed above
110 is accounted for, at least in a crude fashion. In a collection of numerical experiments, the non-
111 linear skeleton model has been shown to simulate realistic MJO events with significant variations
112 in occurrence and strength, asymmetric east-west structures, as well as a preferred localization
113 over the background state warm pool region (Majda and Stechmann, 2011). More recently, a
114 stochastic version of the skeleton model has been developed (Thual et al., 2014). In the stochastic
115 skeleton model, a simple stochastic parametrization allows for an intermittent evolution of the
116 unresolved synoptic-scale convective/wave processes and their planetary envelope. This stochastic
117 parametrization follows a similar strategy found in the related studies mentioned above (e.g. as
118 reviewed in Majda et al., 2008). Most notably, the stochastic skeleton model has been shown to
119 reproduce qualitatively the intermittent growth and demise of MJO wave trains found in nature,
120 i.e. the occurrence of series of successive MJO events, either two, three or sometimes more in a row
121 (Matthews, 2008; Yoneyama et al., 2013).

122 In the present article, we will examine the solutions of a stochastic skeleton model with seasonal
123 cycle. While previous work on the skeleton model has focused essentially on the MJO, we focus
124 here on the tropical intraseasonal variability in general, as discussed above. Two main features of
125 the intraseasonal variability that are qualitatively reproduced by the model are:

- 126 IV. Meridionally asymmetric intraseasonal events, and
- 127 V. A seasonal modulation of intraseasonal variability.

128 Indeed, we will show that the stochastic skeleton model with seasonal cycle reproduces a large
129 diversity of intraseasonal events found in nature, with for example some characteristics reminis-
130 cent of both the MJO and the summer monsoon ISO. This occurs despite the fact that important
131 details such as land-sea contrast, shear, tilted vertical structure, and continental topography are
132 not treated in the model. In addition, we will show that the model reproduces qualitatively the

133 meridional migration of the intraseasonal variability during the year. In order to account for fea-
134 tures (IV-V), two important modifications are considered in the stochastic skeleton model with
135 seasonal cycle. First, while in previous works with the skeleton model focusing on the MJO (Ma-
136 jda and Stechmann, 2009b, 2011; Thual et al., 2014) a single equatorial component of convective
137 heating was considered, here we consider additional off-equatorial components of convective heat-
138 ing in order to further produce meridionally asymmetric intraseasonal events beyond the MJO.
139 Second, a simple seasonal cycle is included that consists of a background warm pool state of
140 heating/moistening that migrates meridionally during the year.

141 The article is organized as follows. In section 2 we recall the design and main features of the
142 skeleton model, and present the stochastic skeleton model with seasonal cycle used here. In section
143 3 we present the main features of the model solutions, including their zonal wavenumber-frequency
144 power spectra and seasonal modulation, as well as several hovmoller diagrams. In section 4 we
145 focus on three interesting types of intraseasonal events found in the model solutions and analyze
146 their potential observational surrogates, their approximate structure and occurrence through the
147 year. Section 5 is a discussion with concluding remarks.

148 **2 Model Formulation**

149 **2.1 Stochastic Skeleton Model**

150 The skeleton model has been proposed originally by Majda and Stechmann (2009b) (hereafter
151 MS2009), and further analyzed in Majda and Stechmann (2011) (hereafter MS2011) and Thual
152 et al. (2014) (hereafter TMS2014). It is a minimal non-linear oscillator model for the MJO and the
153 intraseasonal-planetary variability in general. The design of the skeleton model is briefly recalled
154 here, and the reader is invited to refer to those previous publications for further details.

155 The fundamental assumption in the skeleton model is that the MJO involves a simple multi-
156 scale interaction between (i) planetary-scale dry dynamics, (ii) lower-level moisture q and (iii) the
157 planetary-scale envelope of synoptic-scale convection/wave activity, a . The planetary envelope a in
158 particular is a collective (i.e. integrated) representation of the convection/wave activity occurring

159 at sub-planetary scale (i.e. at synoptic-scale and possibly at mesoscale), the details of which are
 160 unresolved. A key part of the $q - a$ interaction is how moisture anomalies influence convection.
 161 Rather than a functional relationship $a = a(q)$, it is assumed that q influences the tendency (i.e.
 162 the growth and decay rates) of the envelope of synoptic activity:

$$\partial_t a = \Gamma q a, \quad (1)$$

163 where $\Gamma > 0$ is a constant of proportionality: positive (negative) low-level moisture anomalies
 164 create a tendency to enhance (decrease) the envelope of synoptic activity.

165 The basis for equation (1) comes from a combination of observations, modeling, and theory.
 166 Generally speaking, lower-tropospheric moisture is well-known to play a key role in regulating
 167 convection (Grabowski and Moncrieff, 2004; Moncrieff, 2004; Holloway and Neelin, 2009), and has
 168 been shown to lead the MJO's heating anomalies (Kikuchi and Takayabu, 2004; Kiladis et al.,
 169 2005; Tian et al., 2006), which suggests the relationship in equation (1). This relationship is
 170 further suggested by simplified models for synoptic-scale convectively coupled waves showing that
 171 the growth rates of the convectively coupled waves depend on the wave's environment, such as
 172 the environmental moisture content (Khouider and Majda, 2006; Majda and Stechmann, 2009a;
 173 Stechmann et al., 2013). In particular, Stechmann et al. (2013) estimate the value of Γ from these
 174 growth rate variations.

175 In the skeleton model, the $q - a$ interaction parametrized in equation (1) is further combined
 176 with the linear primitive equations projected on the first vertical baroclinic mode. This reads, in
 177 non-dimensional units,

$$\begin{aligned} \partial_t u - yv - \partial_x \theta &= 0 \\ yu - \partial_y \theta &= 0 \\ \partial_t \theta - (\partial_x u + \partial_y v) &= \overline{H}a - s^\theta \\ \partial_t q + \overline{Q}(\partial_x u + \partial_y v) &= -\overline{H}a + s^q \end{aligned} \quad (2)$$

178 with periodic boundary conditions along the equatorial belt. The first three rows of equation (2)
 179 describe the dry atmosphere dynamics, with equatorial long-wave scaling as allowed at planetary
 180 scale. The u and v are the zonal and meridional velocity, respectively, θ is the potential temperature

181 and in addition $p = -\theta$ is the pressure. The fourth row describes the evolution of low-level
182 moisture q . All variables are anomalies from a radiative-convective equilibrium, except a . In
183 order to reconstruct the complete fields having the structure of the first vertical baroclinic mode,
184 one must use $u(x, y, z, t) = u(x, y, t)\sqrt{2}\cos(z)$, $\theta(x, y, z, t) = \theta(x, y, t)\sqrt{2}\sin(z)$, etc., with a slight
185 abuse of notation. This model contains a minimal number of parameters: \bar{Q} is the background
186 vertical moisture gradient, Γ is a proportionality constant. The \bar{H} is irrelevant to the dynamics
187 (as can be seen by rescaling a) but allows us to define a heating/drying rate $\bar{H}a$ for the system
188 in dimensional units. The s^θ and s^q are external sources of cooling and moistening, respectively,
189 that need to be prescribed in the system (see hereafter). The skeleton model depicts the MJO as a
190 neutrally-stable planetary wave. In particular, the linear solutions of the system of equations (1-2)
191 (when a is truncated at the first Hermite function component, see hereafter) exhibit a MJO mode
192 with essential observed features, namely a slow eastward phase speed of roughly 5 m s^{-1} , a peculiar
193 dispersion relation with $d\omega/dk \approx 0$ and a horizontal quadrupole structure (MS2009; MS2011).

194 The stochastic skeleton model, introduced in TMS2014, is a modified version of the skeleton
195 model from equations (1-2) with a simple stochastic parametrization of the synoptic scale pro-
196 cesses. The amplitude equation (1) is replaced by a stochastic birth/death process (the simplest
197 continuous-time Markov process) that allows for intermittent changes in the envelope of synoptic
198 activity (see chapter 7 of Gardiner, 1994; Lawler, 2006). Let a be a random variable taking discrete
199 values $a = \Delta a \eta$, where η is a positive integer. The probabilities of transiting from one state η to
200 another over a time step Δt read as follows:

$$\begin{aligned}
P\{\eta(t + \Delta t) = \eta(t) + 1\} &= \lambda\Delta t + o(\Delta t) \\
P\{\eta(t + \Delta t) = \eta(t) - 1\} &= \mu\Delta t + o(\Delta t) \\
P\{\eta(t + \Delta t) = \eta(t)\} &= 1 - (\lambda + \mu)\Delta t + o(\Delta t) \\
P\{\eta(t + \Delta t) \neq \eta(t) - 1, \eta(t), \eta(t) + 1\} &= o(\Delta t),
\end{aligned}
\tag{3}$$

201 where λ and μ are the upward and downward rates of transition, respectively. They read:

$$\lambda = \begin{cases} \Gamma|q|\eta + \delta_{\eta 0} & \text{if } q \geq 0 \\ \delta_{\eta 0} & \text{if } q < 0 \end{cases} \quad \text{and } \mu = \begin{cases} 0 & \text{if } q \geq 0 \\ \Gamma|q|\eta & \text{if } q < 0 \end{cases} \quad (4)$$

202 where $\delta_{\eta 0}$ is the kronecker delta operator. The above choice of the transition rates ensures that
203 $\partial_t E(a) = \Gamma E(qa)$ for Δa small, where E denotes the statistical expected value, so that the $q - a$
204 interaction described in equation (1) is recovered on average.

205 This stochastic birth/death process allows us to account for the intermittent contribution of
206 unresolved synoptic-scale details on the MJO. The synoptic-scale activity consists of a complex
207 menagerie of convectively coupled equatorial waves, such as 2-day waves, convectively coupled
208 Kelvin waves, etc (Kiladis et al., 2009). Some of these synoptic details are important to the
209 MJO, as they can be both modulated by the planetary background state and contribute to it, for
210 example through upscale convective momentum transport or enhanced surface heat fluxes (Majda
211 and Biello, 2004; Biello and Majda, 2005, 2006; Moncrieff et al., 2007; Majda and Stechmann,
212 2009a; Stechmann et al., 2013). With respect to the planetary processes depicted in the skeleton
213 model, the contribution of those synoptic details appears most particularly to be highly irregular,
214 intermittent, and with a low predictability (e.g. Dias et al., 2013), which is parametrized by
215 equation (3). This stochastic parametrization follows the same prototype found in previous related
216 studies (Majda et al., 2008). The methodology consists in coupling some simple stochastic triggers
217 to the otherwise deterministic processes, according to some probability laws motivated by physical
218 intuition gained (elsewhere) from observations and detailed numerical simulations. Most notably,
219 the stochastic skeleton model has been shown to reproduce qualitatively the intermittent growth
220 and demise of MJO wave trains found in nature, i.e. the occurrence of series of successive MJO
221 events, either two, three or sometimes more in a row (Matthews, 2008; Yoneyama et al., 2013;
222 TMS2014).

2.2 Meridionally Extended Skeleton Model

We now introduce a meridionally extended version of the stochastic skeleton model. Previous work on the skeleton model has focused essentially on the MJO dynamics, associated with an equatorial component of convective heating $\overline{H}a$ (MS2009, MS2011, TMS2014). In order to produce intraseasonal events beyond the MJO, with either a meridionally symmetric or asymmetric structure, we include here additional off-equatorial components of convective heating $\overline{H}a$ in the skeleton model. The meridionally extended skeleton model is efficiently solved using a pseudo-spectral method (i.e. using both spectral space and physical space) that is similar to the one from Majda and Khouider (2001), which is detailed below.

First, we consider a projection of the skeleton model variables from equation (2) on a spectral space consisting of the first M meridional Hermite functions $\phi_m(y)$ (see e.g. Biello and Majda, 2006):

$$a(x, y, t) = \sum_{m=0}^{M-1} A_m(x, t) \phi_m(y), \text{ with} \quad (5)$$

$$\phi_m(y) = \frac{H_m e^{-y^2/2}}{\sqrt{2^m m!} \sqrt{\pi}}, \quad 0 \leq m \leq M-1, \text{ and with Hermite polynomials } H_m(y) = (-1)^m e^{y^2} \frac{d^m}{dy^m} e^{-y^2} \quad (6)$$

This spectral space allows us to easily solve the dry dynamics component of the skeleton model (first three rows of equation 2). A suitable change of variables for this is to introduce K and R_m , $1 \leq m \leq M-2$, that are the amplitudes of the first equatorial Kelvin and Rossby waves, respectively. Their evolution reads:

$$\partial_t K + \partial_x K = -\frac{1}{\sqrt{2}} S_0 \quad (7)$$

$$\partial_t R_m - \frac{\partial_x R_m}{2m+1} = -\frac{2\sqrt{m(m+1)}}{2m+1} (\sqrt{m} S_{m+1} + \sqrt{m+1} S_{m-1}) \quad (8)$$

with $S_m = \overline{H}A_m - S_m^\theta$, $0 \leq m \leq M-1$. The variables from equation (2) can then be reconstructed as:

$$u(x, y, t) = \frac{K}{\sqrt{2}} \phi_0 + \sum_{m=1}^{M-2} \frac{R_m}{4} \left[\frac{\phi_{m+1}}{\sqrt{m+1}} - \frac{\phi_{m-1}}{\sqrt{m}} \right] \quad (9)$$

243

$$\theta(x, y, t) = -\frac{K}{\sqrt{2}}\phi_0 - \sum_{m=1}^{M-2} \frac{R_m}{4} \left[\frac{\phi_{m+1}}{\sqrt{m+1}} + \frac{\phi_{m-1}}{\sqrt{m}} \right] \quad (10)$$

244

$$v(x, y, t) = \frac{S_1}{\sqrt{2}}\phi_0 + \sum_{m=1}^{M-2} \left[\partial_x R_m + \sqrt{m+1} S_{m+1} - \sqrt{m} S_{m-1} \right] \frac{\phi_m}{\sqrt{2}(2m+1)} \quad (11)$$

245 Second, we consider a physical space consisting of an ensemble of M zonal “stochastic strips”
 246 with meridional positions y_l , $-(M-1)/2 \leq l \leq (M-1)/2$ given by the roots $\phi_M(y_l) = 0$ (with
 247 here M odd, though the method is also valid for M even). See figure 1 for the setup with $M = 5$.
 248 The values of the skeleton model variables on such stochastic strips reads:

$$a(x, y_l, t) = a_l(x, t) \quad (12)$$

249 One advantage of using these special points in physical space is that the spectral components A_m
 250 from equation (5) can be computed efficiently as:

$$A_m \approx \sum_{l=-(M-1)/2}^{(M-1)/2} a_l \phi_m(y_l) \bar{G}_l, \text{ with } \bar{G}_l = \frac{1}{M(\phi_{M-1}(y_l))^2}, \quad (13)$$

251 which follows from the Gauss-Hermite quadrature approximation (Majda and Khouider, 2001).
 252 This representation allows us to easily solve the moisture and stochastic component of the skeleton
 253 model (fourth row of equation 2 and equation 3). A suitable change of variables to achieve this
 254 is to introduce $Z = q + \bar{Q}\theta$, in order to solve for each zonal stochastic strip a local system of
 255 equations:

$$\partial_t Z_l = (\bar{Q} - 1) \bar{H} a_l + s_l^q - \bar{Q} s_l^\theta \quad (14)$$

256 as well as the stochastic process from equation (3) for each a_l (or η_l).

257 The spectral and physical space used in the present article are shown in figure 1. We consider
 258 here a meridional truncation $M = 5$ (i.e. 5 Hermite functions/zonal stochastic strips) that retains
 259 the main equatorial Kelvin and Rossby waves that are relevant for symmetric and asymmetric
 260 intraseasonal events (Gill, 1980; Biello and Majda 2005, 2006). This corresponds to one zonal
 261 stochastic strip at the equator and four strips off-equator. The spectral components of heating

262 A_0, A_1, A_2 (with meridional profiles ϕ_0, ϕ_1, ϕ_2 shown in figure 1) may excite the equatorial Kelvin
 263 and first three Rossby waves from equations (7-8). Note that in previous work with the skeleton
 264 model for the MJO only (MS2009, MS2011, and TMS2014) a meridional truncation $M = 1$ was
 265 used, corresponding to a single zonal stochastic strip at the equator with associated component
 266 A_0 exciting the Kelvin and first Rossby symmetric waves.

267 **2.3 Seasonal cycle warm pool**

268 In the present article, we consider a background warm pool state of the meridionally extended
 269 skeleton model from section 2.2 that is seasonally varying. The background warm pool state
 270 migrates meridionally with seasons, in qualitative agreement with observations (Zhang and Dong,
 271 2004). The sources of heating/moisture are balanced and read, in dimensional units ($K.day^{-1}$):

$$272 \quad s^\theta = s^q = (1 - 0.6\cos(2\pi x/L))\exp(-(y - y_C)^2/2), \text{ with} \quad (15)$$

$$y_C = Y \sin(2\pi t/T) \quad (16)$$

273 where L is the equatorial belt length, T is the seasonal cycle period (one year), and $Y =$
 274 900 km . The background warm pool state in equation (15) consists of a maximal region of heat-
 275 ing/moistening that extends from $x \approx 10,000 - 30,000 \text{ km}$ and that is centered around y_c , and a
 276 cold pool elsewhere. In boreal spring/autumn ($y_c = 0$) the background warm pool state is centered
 277 at the equator and its meridional profile matches the one of the Hermite function ϕ_0 shown in figure
 278 1 (e.g. as in MS2011; TMS2014). The background warm pool displaces meridionally during the
 279 year, with its meridional center being $y_c = -Y$ in boreal winter, $y_C = 0$ in boreal spring/autumn,
 280 and $y_c = Y$ in boreal summer. This meridional displacement is qualitatively consistent with the
 281 one found in observations. However, here for simplicity the warm pool displacement is symmetric
 282 with respect to the equator; in nature the warm pool displacement is greater in boreal summer
 283 (around 1000 km north) than in boreal winter (around 600km south, see e.g. figure 4 of Zhang
 284 and Dong, 2004). As a result, a direct comparison of the model solutions with observations must
 285 be considered carefully.

286 The other reference parameters values used in this article are identical to TMS2014. They
 287 read, in non-dimensional units: $\overline{Q} = 0.9$, $\Gamma = 1.66$ ($\approx 0.3 K^{-1}day^{-1}$), $\overline{H} = 0.22$ ($10 Kday^{-1}$), with
 288 stochastic transition parameter $\Delta a = 0.001$. Details on the numerical method used to compute
 289 the simulations can be found in appendix A of TMS2014. In the following sections of this article,
 290 simulation results are presented in dimensional units. The dimensional reference scales are x , y :
 291 1500 km, t : 8 hours, u : $50 m.s^{-1}$, θ , q : 15 K (see TMS2014).

292 **3 Model Solutions**

293 In this article we analyze the dynamics of the stochastic skeleton model with seasonal cycle in a
 294 statistically equilibrated regime. This section presents the main features of the model solutions,
 295 namely their zonal wavenumber-frequency power spectra, seasonal modulation, as well as several
 296 hovmoller diagrams.

297 **3.1 Zonal wavenumber-frequency power spectra**

298 The stochastic skeleton model with seasonal cycle simulates a MJO-like signal that is the dominant
 299 signal at intraseasonal-planetary scale, consistent with observations (Wheeler and Kiladis, 1999).
 300 Figure 2 shows the zonal wavenumber-frequency power spectra of model variables averaged within
 301 $1500km$ south/north as a function of the zonal wavenumber k (in $2\pi/40,000$ km) and frequency ω
 302 (in cpd). The MJO appears here as a power peak in the intraseasonal-planetary band ($1 \leq k \leq 3$
 303 and $1/90 \leq \omega \leq 1/30$ cpd), most prominent in u , q and $\overline{H}a$. This power peak roughly corresponds
 304 to the slow eastward phase speed of $\omega/k \approx 5 ms^{-1}$ with the peculiar relation dispersion $d\omega/dk \approx 0$
 305 found in observations (Wheeler and Kiladis, 1999). Those results are consistent with the ones of
 306 TMS2014 (its figure 2 and 7), though the power spectra are here more blurred in comparison. We
 307 denote hereafter the band $1 \leq k \leq 3$ and $1/90 \leq \omega \leq 1/30$ cpd as the MJO band, which will be
 308 used to filter the model solutions in the next sections.

309 The other features in figure 2 are weaker power peaks near the dispersion curves of a moist
 310 Rossby mode (around $k \approx -2$ and $\omega \approx 1/90$ cpd) and of the dry uncoupled Kelvin and Rossby

311 waves from equation (8) (see MS2009; TMS2014). We note that for an antisymmetric average
312 ($0 - 1500km$ north minus $0 - 1500km$ south) the main feature is a power peak near the dispersion
313 curve of the uncoupled Rossby wave R_2 (not shown).

314 **3.2 Seasonal modulation**

315 The intraseasonal variability in the stochastic skeleton model migrates meridionally during the
316 year, approximatively following the meridional migration of the background warm pool. Figure 3
317 shows the seasonal variations of intraseasonal activity over the warm pool region, as a function of
318 meridional position y . This diagnostic is somewhat similar to the one of Zhang and Dong (2004,
319 figure 4). Figure 3(f) will be described in details in section 4.5.

320 This meridional migration of intraseasonal variability shares some similarities with the one
321 observed in nature (Zhang and Dong, 2004), with overall an increased variability in the northern
322 (southern) hemisphere in boreal summer (winter) as seen for all variables. The present model how-
323 ever considers a qualitative truncation of the planetary-scale circulation to a few main components
324 (see section 2), and as result the meridional displacement of intraseasonal variability is strongly
325 dependent on the meridional shape of the first equatorial Kelvin and Rossby waves. This dis-
326 placement is different for each variable: the variable θ for example shows two strong off-equatorial
327 components that approximatively match the off-equatorial gyres of the first symmetric Rossby wave
328 structure (R_1) from equations (8-11). It is useful here to remember that $\theta = -p$ for the surface
329 pressure p with our crude first baroclinic vertical truncation. The variables u and $\overline{H}a$ show strong
330 equatorial components during the entire year that approximatively match the Kelvin wave struc-
331 ture (K), while the variables v and q show strong off-equatorial components that approximatively
332 match the first antisymmetric Rossby wave structure (R_2).

333 **3.3 $y - t$ Hovmoller diagrams**

334 The stochastic skeleton model with seasonal cycle simulates a large diversity of intraseasonal
335 events, either meridionally symmetric or asymmetric, with a realistic intermittency. Figure 4(a-
336 e) shows the $y - t$ Hovmollers diagrams of the model variables, filtered in the MJO band and

337 considered in a meridional slice at the zonal center of the background warm pool ($x = 20,000 \text{ km}$).
338 Figure 4(f) shows the convective heating \overline{Ha} at different times in order to provide additional
339 examples of intraseasonal events.

340 A new feature of the stochastic skeleton model with seasonal cycle as compared to previous
341 work with the skeleton model (MS2009; MS2011; TMS2014) is the simulation of a large diversity of
342 meridionally symmetric and asymmetric intraseasonal events, beyond the MJO. As seen in figure
343 4 on all model variables the intraseasonal events show a great diversity in meridional structure,
344 localization, strength and lifetime. In figure 4(e-f), there are examples of intraseasonal events
345 (hereafter symmetric events) with equatorial convective heating \overline{Ha} around time 72500 days, 75600
346 days, 79500 days, and of intraseasonal events (hereafter half-quadrupole events) with off-equatorial
347 convective heating around time 74800 days, 77300 days, and 80100 days. Some intraseasonal events
348 (hereafter tilted events) even exhibit apparent meridional propagations of convective heating, for
349 example around time 73000 days, 73800 days, and 81700 days. The symmetric, half-quadrupole
350 and tilted types of events are analyzed in further detail in the next section. In addition, the
351 intraseasonal events in figure 4 are organized into intermittent wave trains with growth and demise,
352 i.e. into series of successive intraseasonal events following a primary intraseasonal event, as seen
353 in nature (Matthews, 2008; Yoneyama et al., 2013; TMS2014). This is an attractive feature of the
354 stochastic skeleton model in generating intraseasonal variability.

355 4 Three types of intraseasonal events

356 Three interesting types of intraseasonal events are found in the solutions of the stochastic skeleton
357 model with seasonal cycle: symmetric events, half-quadrupole events, and tilted events. In this
358 section, we provide examples for each of those types of events and discuss their potential obser-
359 vational surrogates. We then analyze the approximate structures of the three types of event and
360 their occurrence in the model solutions.

361 4.1 Symmetric events

362 Figure 5 shows successive snapshots for an example of a symmetric intraseasonal event (for variables
363 filtered in the MJO band). In figure 5, the symmetric event develops over the warm pool region
364 $x \approx 10,000 - 30,000 \text{ km}$ and propagates eastward at a speed of around 5 ms^{-1} . The symmetric
365 event consists of an equatorial center of convective heating $\overline{H}a$, with leading moisture anomalies
366 q and a surrounding quadrupole vortex structure in θ and the relative vorticity denoted as $\text{curl} =$
367 $\partial_x v - \partial_y u$.

368 The symmetric type of event is representative of MJO composites in nature (Hendon and
369 Salby, 1994). It also has the structure of the MJO mode from MS2009. In figure 5, note in
370 addition that the divergence matches the structure of $\overline{H}a$, consistent with the weak temperature
371 gradient approximation being applied at large scales in the tropics (Sobel et al., 2001; Majda and
372 Klein, 2003). This match is also found for the other types of intraseasonal events (see hereafter).
373 Such approximation is relevant here to analyze a posteriori the simulation results, filtered in the
374 MJO band, but is however not relevant in the full model dynamics (see the discussion in the
375 appendix of MS2011). Note also that the curl has a main contribution from $-\partial_y u$ and very little
376 contribution from $\partial_x v$, as expected from the long-wave approximation (not shown).

377 4.2 Half-quadrupole events

378 Figure 6 shows an example of a half-quadrupole intraseasonal event. The half-quadrupole event
379 consists of an off-equatorial center of convective heating $\overline{H}a$, with leading off-equatorial moisture
380 anomalies q , and a surrounding vortex structure in θ and the curl that is most pronounced in the
381 hemisphere of heating anomalies (i.e. a half-quadrupole). In particular, this event shows strong
382 off-equatorial v anomalies (e.g. as compared to the symmetric event from figure 5).

383 The half-quadrupole type of event may be representative of some intraseasonal convective
384 anomalies in nature that develop off-equator over the western Pacific region (Wang and Rui, 1990;
385 Jones et al., 2004; Izumo et al., 2010; Tung et al., 2014a, b). However, in nature those intraseasonal
386 convective anomalies often follow convective anomalies at the equator in the Indian ocean, that
387 bifurcate either northward (in boreal summer) or southward (in boreal winter) when reaching

388 the maritime continent (Wang and Rui, 1990; Jones et al., 2004). This peculiar behaviour found
389 in nature is sometimes observed in the model solutions when a symmetric event transits to a
390 half-quadrupole event when reaching the warm pool zonal center corresponding to the maritime
391 continent in nature (not shown).

392 The half-quadrupole event shown in figure 6 has maximum anomalies in the northern hemi-
393 sphere. For clarity, we denote this type of event as a half-quadrupole north (HQN) event. There
394 are also examples in the model solutions of half-quadrupole events with maximum anomalies in
395 the southern hemisphere (e.g. at simulation time 74800 days in figure 4), that we denote as
396 half-quadrupole south (HQS) events.

397 4.3 Tilted events

398 Figure 7 shows an example of a tilted intraseasonal event. The tilted event in figure 7 consists of
399 a structure of convective heating $\overline{H}a$ that is oriented north-westward, i.e. tilted, with a similarly
400 tilted leading structure of moisture anomalies q and a tilted quadrupole structure in θ and the
401 curl. This event shows in addition strong cross-equatorial v anomalies.

402 The tilted type of event shows some characteristics that are similar to the ones of the summer
403 monsoon ISO in nature. Due to its tilted structure, the eastward propagation of this type of
404 event (at around 5 ms^{-1}) produces an apparent northward propagation of convective heating (at
405 around 1.5 ms^{-1}) when viewed along a fixed meridional section, similar to Lawrence and Webster
406 (2002). This tilted band of convective heating with apparent northward propagation is one of the
407 salient features of the summer monsoon ISO in nature (Kikuchi et al., 2011), though northward
408 propagation can be sometimes independent of eastward propagation (Webster, 1983; Wang and
409 Rui, 1990; Jiang et al., 2004). In addition, the tilted type of event in the model solutions shows
410 strong cross-equatorial v anomalies and a tilted quadrupole structure that is also found in nature
411 (e.g. Lau and Waliser, 2012, chapt 2 fig 2.10; Lawrence 1999, fig 3.7).

412 The tilted event shown in figure 6 is oriented north-westward, with maximal anomalies in the
413 northern hemisphere. For clarity, we denote this type of event as a tilted north (TN) event. There
414 are also examples of tilted events oriented south-westward with maximal anomalies in the southern

415 hemisphere in the model solutions (e.g. at simulation time 73000 days in figure 4), that we denote
 416 as tilted south (TS) events. Note that there are also examples in the model solutions of tilted
 417 events oriented north-westward (south-westward) in the southern (northern) hemisphere, that are
 418 not considered here (not shown).

419 4.4 Approximate Structures of intraseasonal events

420 Here we provide a simplified description of the structure of the three type of intraseasonal events
 421 (symmetric, half-quadrupole and tilted events) found in the solutions of the stochastic skeleton
 422 model with seasonal cycle. The approximate structure of those events can be retrieved with good
 423 accuracy by considering the atmospheric response to prescribed heating structures $\overline{H}a$ propagating
 424 eastward at constant speed, in a fashion similar to Chao (1987) (see also Biello and Majda, 2005,
 425 2006).

426 We consider prescribed heating anomalies on the equatorial and first northward zonal stochastic
 427 strips of the skeleton model (cf figure 1 and equation 12). This reads, in non-dimensional units:

$$\begin{aligned}
 \overline{H}a_0 - s_0^\theta &= \overline{H}a_E \cos(kx - \omega t) \\
 \overline{H}a_1 - s_1^\theta &= \overline{H}a_N \cos(kx - \omega t - b) \\
 \overline{H}a_l - s_l^\theta &= 0, \quad l = -2, -1, 2
 \end{aligned}
 \tag{17}$$

428 where a_E , a_N , and b are prescribed parameters. For the truncation $M = 5$ adopted in the present
 429 article a_0 is the planetary envelope of synoptic/convective activity on the zonal stochastic strip
 430 $l = 0$ located at the equator, and a_1 is the planetary envelope of synoptic/convective activity on
 431 the zonal stochastic strip $l = 1$ located at around 1500 km north (see figure 1).

432 The above prescribed heating anomalies are considered in the skeleton model from equation
 433 (2) (with the meridional truncation $M = 5$ adopted in the present article), where they replace the
 434 stochastic parametrization from equation (3). We assume steady-state solutions taken in a moving
 435 frame with speed which is approximatively the one of the MJO, $c_F = 5 \text{ m s}^{-1}$; this is obtained by
 436 applying the variable change $\partial_t = -c_F \partial_x$ in equation (2). The approach is similar to the one of
 437 Chao (1987) (see also Biello and Majda, 2005, 2006); however here there is no frictional dissipation

438 and the evolution of lower level moisture q is also considered.

439 Figure 8 (top) shows the prescribed heating and associated atmospheric response for a sym-
440 metric event. For this event, we consider equatorial heating anomalies only: $a_E = 0.06$ (such that
441 $\overline{H}a \approx 0.6 \text{ K day}^{-1}$ at the equator), $a_N = 0$ and $b = 0$. We also choose a wavenumber $k = 1$ in figure
442 8 for illustration. The atmospheric response is overall consistent with the one of the individual
443 event from figure 5, and is in essence the MJO quadrupole vortex structure centered at the equator
444 found in previous works (MS2009).

445 Figure 8 (middle) shows the prescribed heating and atmospheric response for a half-quadrupole
446 north (HQN) event. For this event, we consider off-equatorial convective heating only: $a_E = 0$,
447 $a_N = 0.04$ with no phase shift so $b = 0$. The atmospheric response, located in the northern
448 hemisphere, is overall consistent with the one of the individual event from figure 6, with strong off-
449 equatorial θ , q and v anomalies. Note that a half-quadrupole south (HQS) event would be retrieved
450 by considering off-equatorial heating on the southern strip $l = -1$ instead of the northern strip
451 $l = 1$.

452 Figure 8 (bottom) shows the prescribed heating and associated atmospheric response for a
453 tilted north (TN) event. For this tilted event, we consider a combination of both equatorial and
454 off-equatorial convective heatings, that are taken out of phase in order to produce a tilted band
455 of convective heating oriented north-westward in the northern hemisphere: $a_E = 0.04$, $a_N = a_E$,
456 with a phase shift $b = -\pi/2$. The atmospheric response is overall consistent with the one of the
457 individual event from figure 7, with a tilted leading structure of moisture anomalies q , a tilted
458 quadrupole structure in the curl and strong cross-equatorial v anomalies. Note that a tilted south
459 (TS) event would be retrieved by considering off-equatorial heating on the southern strip $l = -1$
460 instead of the northern strip $l = 1$.

461 4.5 Indices of intraseasonal events

462 In this subsection we derive indices that estimate the amplitude of the specific types of intraseasonal
463 events (symmetric, half-quadrupole and tilted events) found in the solutions of the stochastic
464 skeleton model with seasonal cycle. Those indices allow one to track the occurrence of each type of

465 event through the year. The model reproduces in particular a realistic alternance of the occurrence
 466 of half-quadrupole and tilted events between boreal summer/winter, as well symmetric events
 467 overall most prominent during the year.

468 The definition of each index is motivated from the approximate structure of individual events
 469 presented in section 4.4. Each index is computed from the component of convective heating \overline{Ha}
 470 over one or various zonal stochastic strips, filtered in the MJO band. For symmetric events the
 471 index is \overline{Ha}_0 , namely the \overline{Ha} component on the zonal stochastic strip $l = 0$ located at the equator
 472 (see figure 1). For half-quadrupole north (HQN) events the index is \overline{Ha}_1 , while for half-quadrupole
 473 south (HQS) events the index is \overline{Ha}_{-1} . For tilted north (TN) events the index is $(\overline{Ha}_0 + \overline{Ha}_1^*)/2$
 474 , where a_1^* is the \overline{Ha} component on the northern zonal stochastic strip $l = 1$ shifted eastward by
 475 90 degrees for each wavenumber $k = 1, 2, 3$, in a fashion similar to equation (17) and figure 8. For
 476 tilted south (TS) events the index is similarly $(\overline{Ha}_0 + \overline{Ha}_{-1}^*)/2$.

477 Figure 9 shows the longitude-time hovmoller diagrams of each index compared to a $y - t$
 478 Hovmoller diagram of \overline{Ha} (identical to the one in figure 4e). This representation allows to track
 479 the occurrence of each type of event in the simulations. As shown in figure 9, symmetric events are
 480 overall most prominent. The strong tilted events at simulation time 73000 days and 73800 days in
 481 particular are well captured by the associated indices, though a drawback of the present method
 482 is that they are also counted as symmetric and half-quadrupole events.

483 The above indices also allow to diagnose the occurrence of each type of intraseasonal event
 484 through the year. Figure 3(f) shows the occurrence of each type of event, as a function of seasons.
 485 The occurrence of each type of event is computed based on a threshold criteria: we compute for
 486 each index a threshold criteria that is equal to unity when the index magnitude from figure 9 is
 487 superior to a threshold value set here at $0.2 Kday^{-1}$, and zero otherwise. The threshold criteria is
 488 then averaged over the warm pool region ($x = 10, 000$ to $30, 000 km$) and over each day of the
 489 year, which is shown in figure 3(f).

490 The occurrence of each type of intraseasonal event shown in figure 3(f) is qualitatively consistent
 491 with the one found in nature. In particular, half-quadrupole north (HQN) and tilted north (TN)
 492 events are most prominent in boreal summer as compared to boreal winter, while half-quadrupole

493 south (HQS) and tilted south (TS) events are most prominent in boreal winter as compared to
494 boreal summer (Wang and Rui, 1990; Jones et al., 2004). Meanwhile, the symmetric events are
495 most prominent through the entire year as compared to the other types of events. This is consistent
496 with observations where MJO events are most prominent through the year, except during boreal
497 summer where summer monsoon ISO (i.e. tilted north) events are most prominent (Lawrence and
498 Webster, 2002; Kikuchi et al., 2011).

499 5 Conclusions

500 We have analyzed the dynamics of a stochastic skeleton model for the MJO and the intraseasonal-
501 planetary variability in general with a seasonal cycle. It is a modified version of a minimal dy-
502 namical model, the skeleton model (Majda and Stechmann, 2009b, 2011; Thual et al., 2014). The
503 skeleton model has been shown in previous work to capture together the MJO’s salient features
504 of (I) a slow eastward phase speed of roughly 5ms^{-1} , (II) a peculiar dispersion relation with
505 $d\omega/dk \approx 0$, and (III) a horizontal quadrupole structure. Its stochastic version further includes
506 a simple stochastic parametrization of the unresolved synoptic-scale convective/wave processes.
507 Most notably, the stochastic skeleton model has been shown to reproduce qualitatively the inter-
508 mittent growth and demise of MJO wave trains found in nature. In the present article, we further
509 focus on the tropical intraseasonal variability in general simulated by the stochastic skeleton model.
510 Two main features of the intraseasonal variability that are qualitatively reproduced by the model
511 are:

512 IV. Meridionally asymmetric intraseasonal events, and

513 V. A seasonal modulation of intraseasonal variability.

514 In order to account for features (IV-V), two important modifications have been considered in the
515 stochastic skeleton model with seasonal cycle. First, while in previous works with the skeleton
516 model focusing on the MJO (Majda and Stechmann, 2009b, 2011; Thual et al., 2014) a single
517 equatorial component of convective heating was considered, here we have considered additional off-
518 equatorial components of convective heating in order to further produce meridionally asymmetric

519 intraseasonal events beyond the MJO. Second, a simple seasonal cycle has been included that
520 consists in a background warm pool state of heating/moistening that migrates meridionally during
521 the year.

522 A new feature of the stochastic skeleton model with seasonal cycle, as compared to previous
523 works with the skeleton model, is the simulation of a large diversity of meridionally symmetric and
524 asymmetric intraseasonal-planetary events. Indeed, in nature intraseasonal events show a great
525 diversity in horizontal structure, strength, lifetime and localization (Wang and Rui, 1990; Jones
526 et al., 2004; Masunaga, 2007). For example, both equatorial and off-equatorial convective heating
527 coexist during intraseasonal events with characteristics and intensity that differ from one event
528 to another, including during MJO events (Tung et al., 2014a, b; Biello and Majda, 2005, 2006).
529 The present stochastic skeleton model with seasonal cycle qualitatively reproduces this diversity of
530 intraseasonal events. In addition, despite their diversity those intraseasonal events are organized
531 into intermittent wave trains with growth and demise, i.e. into series of successive events following
532 a primary intraseasonal event, as seen in nature (Matthews, 2008; Yoneyama et al., 2013; Thual
533 et al., 2014). This is an attractive feature of the stochastic skeleton model with seasonal cycle in
534 generating intraseasonal variability.

535 While the stochastic skeleton model with seasonal cycle obviously lacks several key physical
536 processes in order to account for the complete dynamics of the MJO and intraseasonal variability
537 in general, e.g. topographic effects, land-sea contrast, a refined vertical structure, mean vertical
538 shears, etc (Lau and Waliser, 2012 chapt 10, 11), it is interesting that some aspects of peculiar
539 intraseasonal events found in nature are qualitatively recovered in the model solutions. Three inter-
540 esting types of intraseasonal-planetary events found in the model solutions are symmetric events,
541 half-quadrupole events, and tilted events. As regards observations, the symmetric events with
542 quadrupole vortex structure are most representative of MJO composites (Hendon and Salby, 1994;
543 Majda and Stechmann, 2009b). The half-quadrupole events, with off-equatorial heating structure
544 may be representative of some intraseasonal convective anomalies that develop off-equator in the
545 western Pacific, though in nature those convective anomalies often follow convective anomalies at
546 the equator in the Indian ocean (Wang and Rui, 1990; Jones et al., 2004; Izumo et al., 2010; Tung

547 et al., 2014a, b). Finally, the tilted events with a heating structure oriented north-westward and
548 strong cross-equatorial flow share some characteristics with the summer monsoon intraseasonal
549 oscillation: in particular, the eastward propagation of those events (at around 5 m s^{-1}) results
550 in apparent northward propagations (at around 1.5 m s^{-1}) when viewed along a latitudinal sec-
551 tion, similar to Lawrence and Webster (2002). Note in addition that there are other types of
552 intraseasonal events simulated by the stochastic skeleton model with seasonal cycle that have not
553 been analyzed in detail here. Some events simulated by the present model are for example of a
554 mixed type, i.e. result from a combination of the three above types of events, or transit from
555 one event type to another during their lifetime. This includes examples of intraseasonal events
556 transiting from a symmetric event to a half-quadrupole event when reaching the warm pool center
557 corresponding to the maritime continent in nature (Wang and Rui, 1990; Jones et al., 2004).

558 The intraseasonal-planetary variability in nature migrates meridionally during the year, ap-
559 proximately following the migration of warm sea surface temperatures (Salby and Hendon, 1994;
560 Zhang and Dong, 2004). This feature is qualitatively recovered by the stochastic skeleton model
561 with seasonal cycle, despite the fact that the present model considers a qualitative truncation of
562 the planetary-scale circulation to a few main components. For example, the meridional displace-
563 ment is different for each variable, which is related to the meridional shape of the few equatorial
564 Kelvin and Rossby waves considered here (cf section 2). Nevertheless the model exhibits a strong
565 off-equatorial intraseasonal variability in both boreal summer and winter, with potential impli-
566 cations for understanding its interactions with the Asian and Australian monsoon (Wheeler and
567 Hendon, 2004; Lau and Waliser, 2012 chapt 2, 5). In addition, we have verified that the occurrence
568 of the three above types of intraseasonal events during the year is qualitatively consistent with
569 observations. For instance, tilted events with heating structure oriented north-westward and half-
570 quadrupole events with northern off-equatorial heating structure are more prominent in boreal
571 summer as compared to the other seasons (Wang and Rui, 1990; Jones et al., 2004). Meanwhile,
572 symmetric events are the most prominent type of event through the entire year, consistent with
573 observations where MJO events are most prominent through the year except during boreal summer
574 where summer monsoon ISO (i.e. tilted north) events are most prominent (Lawrence and Webster,

575 2002; Kikuchi et al., 2011).

576 While the skeleton model appears to be a plausible representation for the essential mechanisms
577 of the MJO and some aspects of intraseasonal variability in general, several issues need to be
578 adressed as a perspective for future work. One important issue is to compare further the skeleton
579 model solutions with their observational surrogates, qualitatively and also quantitatively. A more
580 complete model should also account for more detailed sub-planetary processes within the envelope
581 of intraseasonal events, including for example synoptic-scale convectively coupled waves and/or
582 mesoscale convective systems (e.g. Moncrieff et al., 2007; Majda et al., 2007; Khouider et al.,
583 2010; Frenkel et al., 2012).

584 **Acknowledgements:** The research of A.J.M. is partially supported by the Office of Naval
585 Research Grant ONR MURI N00014 -12-1-0912. The research of S.N.S. is partially supported by
586 the Office of Naval Research Grants ONR YIP N00014-12-1-0744 and ONR MURI N00014-12-1-
587 0912. S.T. is supported as a postdoctoral fellow through A.J.M's ONR MURI Grant.

588 References

589 Ajayamohan, R. S., Khouider, B., and Majda, A. J. (2013). Realistic initiation and dynamics
590 of the Madden-Julian Oscillation in a coarse resolution aquaplanet GCM. *Geophys. Res. Lett.*,
591 40:6252–6257.

592 Annamalai, H. and Sperber, K. R. (2005). Regional Heat Sources and the Active and Break Phases
593 of Boreal Summer Intraseasonal (30-50 Day) Variability. *J. Atmos. Sci.*, 62:2726–2748.

594 Biello, J. A. and Majda, A. J. (2005). A new multiscale model for the madden-julian oscillation.
595 *J. Atmos. Sci.*, 62(6):1694–1721.

596 Biello, J. A. and Majda, A. J. (2006). Modulating synoptic scale convective activity and boundary
597 layer dissipation in the IPESD models of the Madden-Julian oscillation. *Dyn. Atm. Oceans*,
598 42(1-4):152–215.

- 599 Chao, W. C. (1987). On the origin of the tropical intraseasonal oscillation. *J. Atmos. Sci.*,
600 44(15):1940–1949.
- 601 Deng, Q., Khouider, B., and Majda, A. J. (2014). The MJO in a Coarse-Resolution GCM with a
602 Stochastic Multicloud Parameterization. *J. Atmos. Sci.* submitted.
- 603 Dias, J., Leroux, S., Tulich, S. N., and Kiladis, G. N. (2013). How systematic is organized tropical
604 convection within the MJO? *Geophys. Res. Lett.*, 40:1420–1425.
- 605 Frenkel, Y., Majda, A. J., and Khouider, B. (2012). Using the stochastic multicloud model to
606 improve tropical convective parameterization: A paradigm example. *J. Atmos. Sci.*, 69(3):1080–
607 1105.
- 608 Gardiner, C. W. (1994). *Handbook of stochastic methods for physics, chemistry, and the natural*
609 *sciences*. Springer.
- 610 Gill, A. (1980). Some simple solutions for heat-induced tropical circulation. *Quart. J. Roy. Meteor.*
611 *Soc.*, 106:447–462.
- 612 Goswami, B. N., Ajayamohan, R. S., Xavier, P. K., and Sengupta, D. (2003). Clustering of
613 synoptic activity by Indian summer monsoon intraseasonal oscillations. *Geophys. Res. Lett.*,
614 8:1–14. doi:10.1029/2002GL016734.
- 615 Grabowski, W. W. and Moncrieff, M. W. (2004). Moisture-convection feedback in the Tropics.
616 *Quart. J. Roy. Meteor. Soc.*, 130:3081–3104.
- 617 Hendon, H. H. and Liebmann, B. (1994). Organization of convection within the Madden-Julian
618 oscillation. *J. Geophys. Res.*, 99:8073–8083.
- 619 Hendon, H. H. and Salby, M. L. (1994). The life cycle of the madden-julian oscillation. *J. Atmos.*
620 *Sci.*, 51(15):2225–2237.
- 621 Holloway, C. E. and Neelin, J. D. (2009). Moisture Vertical Structure, Column Water Vapor, and
622 Tropical Deep Convection. *J. Atmos. Sci.*, 66:1665–1683.

623 Hung, M.-P., Lin, J.-L., Wang, W., Kim, D., Shinoda, T., and Weaver, S. J. (2013). Mjo and
624 convectively coupled equatorial waves simulated by cmip5 climate models. *J. Climate*, 26:6185–
625 6214.

626 Izumo, T., Masson, S., Vialard, J., de Boyer Montegut, C., Behera, S. K., Madec, G., Takahashi,
627 K., and Yamagata, T. (2010). Low and high frequency Madden-Julian oscillations in austral
628 summer: interannual variations. *Clim. Dyn.*, 35:669–683.

629 Jiang, X., Li, T., and Wang, B. (2004). Structures and mechanisms of the northward propagating
630 boreal summer intraseasonal oscillation. *J. Climate*, 17:1022–1039.

631 Jones, C., Carvalho, L. M., Higgins, R. W., Waliser, D. E., and Schemm, J.-K. E. (2004). Clima-
632 tology of Tropical Intraseasonal Convective Anomalies: 1979-2002. *J. Climate*, 17:523–539.

633 Khouider, B., Biello, J. A., and Majda, A. J. (2010). A stochastic multicloud model for tropical
634 convection. *Comm. Math. Sci.*, 8(1):187–216.

635 Khouider, B. and Majda, A. J. (2006). A simple multicloud parametrization for convectively
636 coupled tropical waves. Part I: Linear Analysis. *J. Atmos. Sci.*, 63:1308–1323.

637 Khouider, B., St-Cyr, A., Majda, A. J., and Tribbia, J. (2011). The MJO and convectively coupled
638 waves in a coarse-resolution GCM with a simple multicloud parameterization. *J. Atmos. Sci.*,
639 68(2):240–264.

640 Kikuchi, K. and Takayabu, Y. N. (2004). The development of organized convection associated
641 with the MJO during TOGA COARE IOP: Trimodal characteristics. *Geophys. Res. Lett.*, 31.
642 L10101,doi:10.1029/2004GL019601.

643 Kikuchi, K., Wang, B., and Kajikawa, Y. (2011). Bimodal representation of the tropical intrasea-
644 sonal oscillation. *Clim. Dyn.* DOI 10.1007/s00382-011-1159-1.

645 Kiladis, G. N., Straub, K. H., and T., H. P. (2005). Zonal and vertical structure of the Madden-
646 Julian oscillation. *J Atmos Sci*, 62:2790–2809.

647 Kiladis, G. N., Wheeler, C., Haertel, P. T., Straub, K. H., and Roundy, P. E. (2009). Convectively
648 coupled equatorial waves. *Rev. Geophys.*, 47. RG2003, doi:10.1029/2008RG000266.

649 Kim, D., K., S., Stern, W., Waliser, D., Kang, I.-S., Maloney, E., Wang, W., Weickmann, K.,
650 Benedict, J., Khairoutdinov, M., Lee, M.-I., Neale, R., Suarez, M., Thayer-Calder, K., and
651 Zhang, G. (2009). Application of MJO simulation diagnostics to climate models. *J. Climate*,
652 22:6413–6436.

653 Lau, K.-M. and Peng, L. (1990). Origin of Low Frequency (Intraseasonal) Oscillations in the
654 Tropical Atmosphere. Part III: Monsoon Dynamics. *J. Atmos. Sci.*, 47:1443–1462.

655 Lau, W. M. and Waliser, D. E. (2012). *Intraseasonal Variability in the Atmosphere-Ocean Climate*
656 *System*. Springer. 642pp.

657 Lawler, G. F. (2006). *Introduction to Stochastic Processes*. CRC Press.

658 Lawrence, D. M. and Webster, P. J. (2002). The boreal summer intraseasonal oscillation: Rela-
659 tionship between northward and eastward movement of convection. *J. Atmo. Sci.*, 59:1593–1606.

660 Lawrence, M. (1999). Intraseasonal Variability of the South Asian Monsoon. *PhD thesis*. 195pp.

661 Lin, J.-L., Kiladis, G. N., Mapes, B. E., Weickmann, K. M., Sperber, K. R., Lin, W., Wheeler,
662 M. C., Schubert, S. D., Del Genio, A., Donner, L. J., Emori, S., Gueremy, J.-F., Hourdin, F.,
663 Rasch, P. J., Roeckner, E., and Scinocca, J. F. (2006). Tropical intraseasonal variability in 14
664 IPCC AR4 climate models. part i: Convective signals. *J. Climate*, 19(12):2665–2690.

665 Madden, R. E. and Julian, P. R. (1971). Detection of a 40-50 day oscillation in the zonal wind in
666 the tropical Pacific. *J. Atmos. Sci.*, 28:702–708.

667 Madden, R. E. and Julian, P. R. (1994). Observations of the 40-50 day tropical oscillation-A
668 review. *Mon. Wea. Rev.*, 122:814–837.

669 Majda, A. J. and Biello, J. A. (2004). A multiscale model for tropical intraseasonal oscillations.
670 *Proc. Natl. Acad. Sci. USA*, 101(14):4736–4741.

671 Majda, A. J., Franzke, C., and Khouider, B. (2008). An applied mathematics perspective on
672 stochastic modelling for climate. *Philos. Trans.Roy. Soc.*, A366(1875):2427–2453.

673 Majda, A. J. and Khouider, B. (2001). A numerical strategy for efficient modeling of the equatorial
674 wave guide. *Proc. Natl. Acad. Sci. USA*, 98(4):1341–1346.

675 Majda, A. J. and Klein, R. (2003). Systematic Multi-Scale Models for the Tropics. *J. Atmos. Sci.*,
676 60:357–372.

677 Majda, A. J. and Stechmann, S. N. (2009a). A simple dynamical model with features of convective
678 momentum transport. *J. Atmos. Sci.*, 66(2):373–392.

679 Majda, A. J. and Stechmann, S. N. (2009b). The skeleton of tropical intraseasonal oscillations.
680 *Proc. Natl. Acad. Sci. USA*, 106(21):8417–8422.

681 Majda, A. J. and Stechmann, S. N. (2011). Nonlinear dynamics and regional variations in the
682 MJO skeleton. *J. Atmos. Sci.*, 68(12):3053–3071.

683 Majda, A. J., Stechmann, S. N., and Khouider, B. (2007). Madden-Julian oscillation analog and
684 intraseasonal variability in a multcloud model above the equator. *Proc. Natl. Acad. Sci. USA*,
685 104:9919–9924.

686 Masunaga, H. (2007). Seasonality and Regionality of the Madden-Julian Oscillation, Kelvin Wave,
687 and Equatorial Rossby Wave. *J. Atmos. Sci.*, 64:4400–4416.

688 Matthews, A. J. (2008). Primary and successive events in the Madden-Julian Oscillation. *Quart.*
689 *J. Roy. Meteor. Soc.*, 134:439–453.

690 Moncrieff, M. (2004). Analytic representation of the large-scale organization of tropical convection.
691 *Quart. J. Roy. Meteor. Soc.*, 130:1521–1538.

692 Moncrieff, M. W., Shapiro, M., Slingo, J., and Molteni, F. (2007). Collaborative research at the
693 intersection of weather and climate. *WMO Bull.*, 56:204–211.

694 Salby, M. L. and Hendon, H. H. (1994). Intraseasonal behavior of clouds, temperature, and winds
695 in the tropics. *J. Atmos. Sci.*, (51):2207–2224.

- 696 Sobel, A. H., Nilsson, J., and Polvani, L. M. (2001). The Weak Temperature Gradient Approximation and Balanced Tropical Moisture Waves. *J. Atmos. Sci.*, 58:3650–3665.
- 697
- 698 Stechmann, S., Majda, A. J., and Skjorshammer, D. (2013). Convectively coupled wave-environment interactions. *Theor. Comput. Fluid Dyn.*, 27:513–532.
- 699
- 700 Stechmann, S. N. and Neelin, J. D. (2011). A stochastic model for the transition to strong convection. *J. Atmos. Sci.*, 68(12):2955–2970.
- 701
- 702 Straub, K. H. and Kiladis, G. N. (2003). Interactions between the Boreal Summer Intraseasonal Oscillation and Higher-Frequency Tropical Wave Activity. *Mon. Wea. Rev.*, 131:945–960.
- 703
- 704 Thual, S., Majda, A. J., and Stechmann, S. N. (2014). A stochastic skeleton model for the MJO. *J. Atmos. Sci.*, 71:697–715.
- 705
- 706 Tian, B., Waliser, D., Fetzer, E., Lambrigsten, B., Yung, Y., and Wang, B. (2006). Vertical moist thermodynamic structure and spatial-temporal evolution of the MJO in AIRS observations. *J. Atmos. Sci.*, 63:2462–2485.
- 707
- 708
- 709 Tung, W.-W., Giannakis, D., and Majda, A. J. (2014a). Symmetric and antisymmetric convection signals in the Madden-Julian oscillation. Part I: Basic modes in infrared brightness temperature. *J. Atmos. Sci.*, *submitted*.
- 710
- 711
- 712 Tung, W.-W., Giannakis, D., and Majda, A. J. (2014b). Symmetric and antisymmetric convection signals in the Madden-Julian oscillation. Part II: Kinematics and thermodynamics. *J. Atmos. Sci.*, *submitted*.
- 713
- 714
- 715 Wang, B. and Rui, H. (1990). Synoptic Climatology of Transient Tropical Intraseasonal Convection Anomalies: 1975-1985. *Meteorol. Atmos. Phys.*, 44:43–61.
- 716
- 717 Wang, B. and Xie, X. (1997). A model for the boreal summer intraseasonal oscillation. *J. Atmos. Sci.*, 54:72–86.
- 718
- 719 Webster, P. J. (1983). Mechanisms of Monsoon Low-Frequency Variability: Surface Hydrological Effects. *J. Atmos. Sci.*, 40:2110–2124.
- 720

- 721 Wheeler, M. and Kiladis, G. N. (1999). Convectively coupled equatorial waves: Analysis of clouds
722 and temperature in the wavenumber-frequency domain. *J. Atmos. Sci.*, 56(3):374–399.
- 723 Wheeler, M. C. and Hendon, H. H. (2004). An all-season real-time multivariate mjo index: Devel-
724 opment of an index for monitoring and prediction. *Mon. Wea. Rev.*, 132:1917–1932.
- 725 Yoneyama, K., Zhang, C., and Long, C. N. (2013). Tracking Pulses of the Madden-Julian Oscilla-
726 tion. *Bull. Am. Meteor. Soc.*, 94:1871–1891.
- 727 Zhang, C. (2005). Madden-julian oscillation. *Rev. Geophys.*, 43. RG2003,
728 doi:10.1029/2004RG000158.
- 729 Zhang, C. and Dong, M. (2004). Seasonality in the madden-julian oscillation. *J. Climate.*, 17:3169–
730 3180.

731 **Figure Captions:**

732 Figure 1: Model spectral and physical space and warm pool shape: Hermite functions ϕ_m , $m =$
733 $0, 1, 2$ (lines) and zonal strips positions y_l , $-(M - 1)/2 \leq l \leq (M - 1)/2$ (dots) for a truncation
734 $M = 5$, as a function of y in 1000km.

735 Figure 2: Zonal wavenumber-frequency power spectra: for (a) u ($m.s^{-1}$), (b) θ (K), (c) q
736 (K), and (d) \overline{Ha} ($Kday^{-1}$), as a function of zonal wavenumber (in $2\pi/40000km$) and frequency
737 (in cpd). The contour levels are in the base 10-logarithm, for the dimensional variables averaged
738 within 1500 km south/north. The black dashed lines mark the periods 90 and 30 days.

739 Figure 3: Intraseasonal activity: for (a) u ($m.s^{-1}$), (b) v ($m.s^{-1}$), (c) θ (K), (d) q (K), and (e)
740 \overline{Ha} ($K.day^{-1}$), as a function of season (month of the year) and meridional position y (1000 km).
741 The intraseasonal activity is computed as the standard deviation of signals filtered in the MJO
742 band ($1 \leq k \leq 3$ and $1/90 \leq \omega \leq 1/30$ cpd) averaged over the warm pool region ($x = 10, 000$ to
743 $30, 000 km$). (f): Occurrence of each type of intraseasonal event: for half-quadrupole south (HQS,
744 blue), tilted south (TS, green), symmetric (black), tilted north (TS, magenta), and half-quadrupole
745 north (HQN, red) events, nondimensional and as a function of season (month of the year, x-axis).

746 Figure 4: $y - t$ Hovmoller diagrams: for (a) u ($m.s^{-1}$), (b) v ($m.s^{-1}$), (c) θ (K), (d) q (K),
747 and (e) \overline{Ha} ($K.day^{-1}$), as a function of meridional position location y (in 1000 km) and simulation
748 time (in 1000 days). (f) repeats the Hovmoller diagram for \overline{Ha} at different times. The variables
749 are filtered in the MJO band ($1 \leq k \leq 3$ and $1/90 \leq \omega \leq 1/30$ cpd), and considered at the warm
750 pool zonal center ($x = 20, 000 km$). The meridional position y_C of the warm pool center, varying
751 with seasons, is overplotted (black line).

752 Figure 5: $x - y$ Snapshots for a symmetric intraseasonal event: for (a) u ($m.s^{-1}$), (b) v ($m.s^{-1}$),
753 (c) θ (K), (d) q (K), (e) \overline{Ha} ($Kday^{-1}$), (f) divergence $\partial_x u + \partial_y v$ ($m.s^{-1})(1000km)^{-1}$, and (g) curl
754 $\partial_x v - \partial_y u$ ($m.s^{-1})(1000km)^{-1}$, as a function of zonal position x (1000km) and meridional position
755 y (1000km). Left label indicates simulation time for each snapshot (in days). The variables are
756 filtered in the MJO band ($1 \leq k \leq 3$ and $1/90 \leq \omega \leq 1/30$ cpd).

757 Figure 6: $x - y$ Snapshots for a half-quadrupole north (HQN) intraseasonal event (see legend
758 of figure 5).

759 Figure 7: $x - y$ Snapshots for a tilted north (TN) intraseasonal event (see legend of figure 5).

760 Figure 8: Atmospheric response to prescribed heating: for (a) u (ms^{-1}), (b) v (ms^{-1}), (c)
761 θ (K), (d) q (K), (e) \overline{Ha} ($Kday^{-1}$), (f) divergence $\partial_x u + \partial_y v$ ($m.s^{-1})(1000km)^{-1}$, and (g) curl
762 $\partial_x v - \partial_y u$ ($m.s^{-1})(1000km)^{-1}$, as a function of zonal position x (1000km) and meridional position
763 y (1000km). This is shown for (top) a symmetric event, (middle) a half-quadrupole north (HQN)
764 event, (bottom) a tilted north (TN) event.

765 Figure 9: (a) $y - t$ Hovmoller diagram: for \overline{Ha} ($Kday^{-1}$), as a function of meridional position
766 location y (in 1000 km) and simulation time (in 1000 days), considered at the warm pool zonal
767 center ($x = 20,000 km$). (b-f): $x - t$ Hovmoller diagrams: for the index of (b) half-quadrupole
768 south (HQS), (c) tilted south (TS), (d) symmetric, (e) tilted north (TN), and (f) half-quadrupole
769 north (HQN) events, in $Kday^{-1}$ and as a function of zonal position location x (in 1000 km) and
770 simulation time (1000 days).

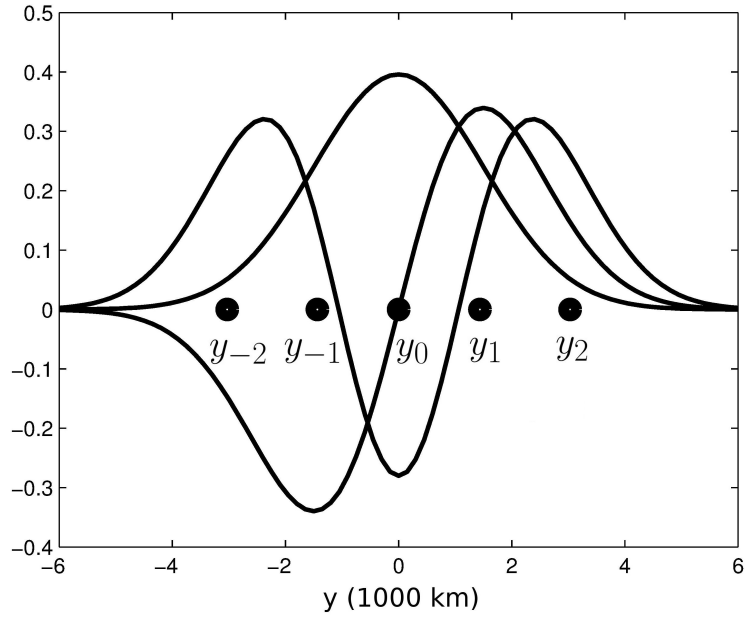


Figure 1: Model spectral and physical space and warm pool shape: Hermite functions ϕ_m , $m = 0, 1, 2$ (lines) and zonal strips positions y_l , $-(M - 1)/2 \leq l \leq (M - 1)/2$ (dots) for a truncation $M = 5$, as a function of y in 1000km.

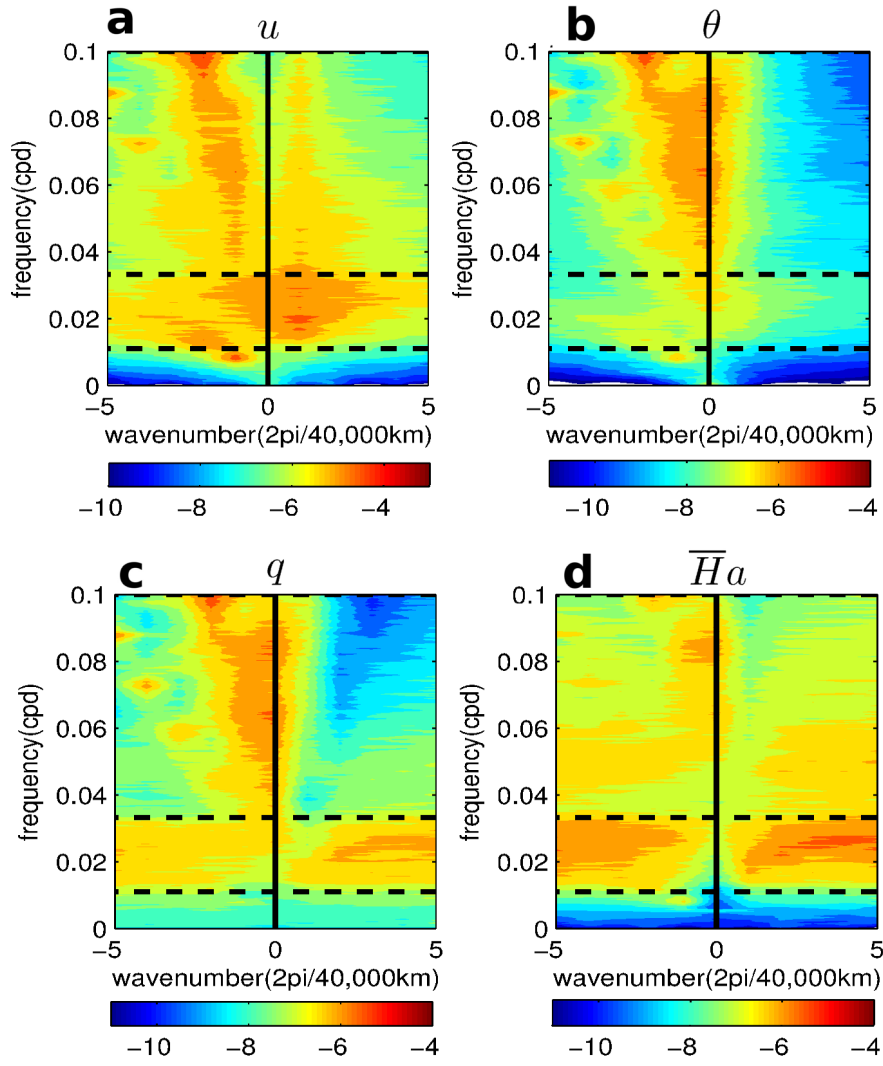


Figure 2: Zonal wavenumber-frequency power spectra: for (a) u (ms^{-1}), (b) θ (K), (c) q (K), and (d) \overline{Ha} ($Kday^{-1}$), as a function of zonal wavenumber (in $2\pi/40000km$) and frequency (in cpd). The contour levels are in the base 10-logarithm, for the dimensional variables averaged within $1500 km$ south/north. The black dashed lines mark the periods 90 and 30 days.

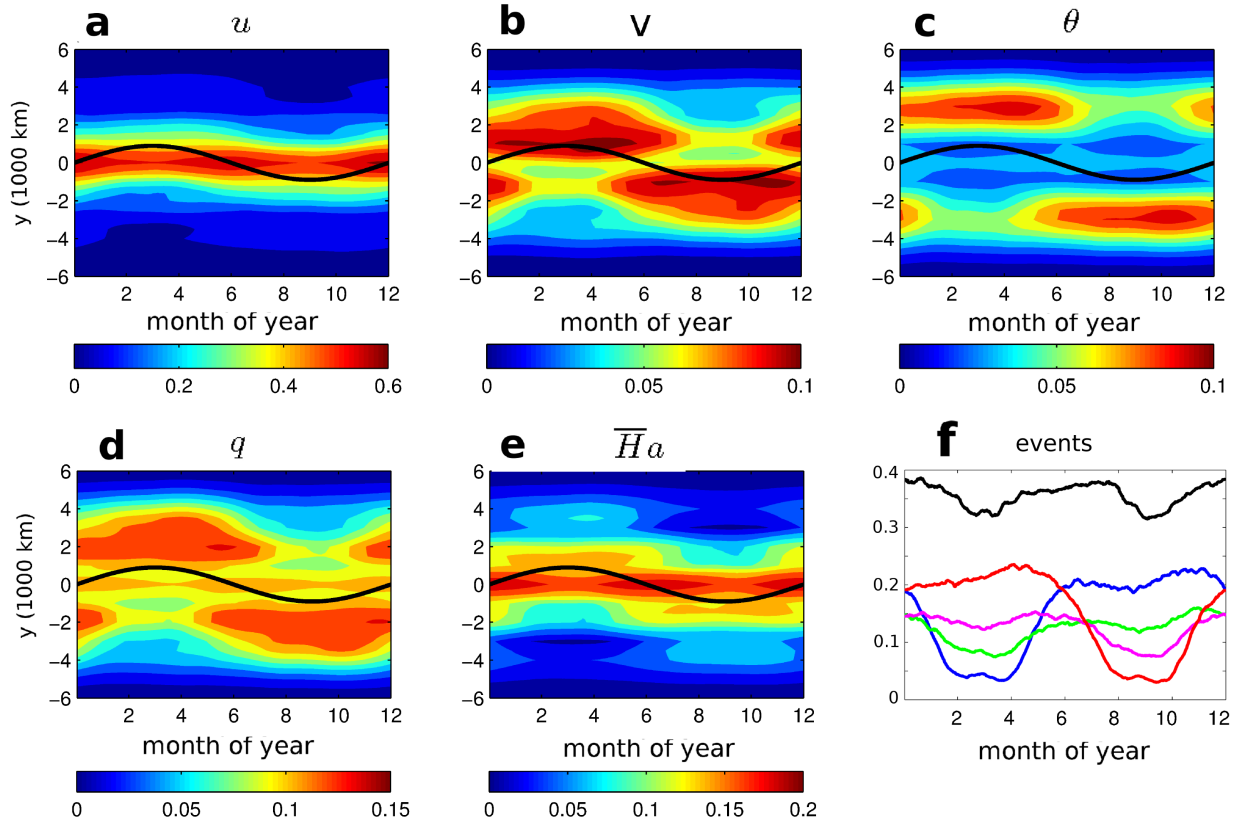


Figure 3: Intraseasonal activity: for (a) u ($m.s^{-1}$), (b) v (ms^{-1}), (c) θ (K), (d) q (K), and (e) \overline{Ha} ($K.day^{-1}$), as a function of season (month of the year) and meridional position y (1000 km). The intraseasonal activity is computed as the standard deviation of signals filtered in the MJO band ($1 \leq k \leq 3$ and $1/90 \leq \omega \leq 1/30$ cpd) averaged over the warm pool region ($x = 10,000$ to $30,000$ km). (f): Occurrence of each type of intraseasonal event: for half-quadrupole south (HQS, blue), tilted south (TS, green), symmetric (black), tilted north (TS, magenta), and half-quadrupole north (HQN, red) events, nondimensional and as a function of season (month of the year, x-axis).

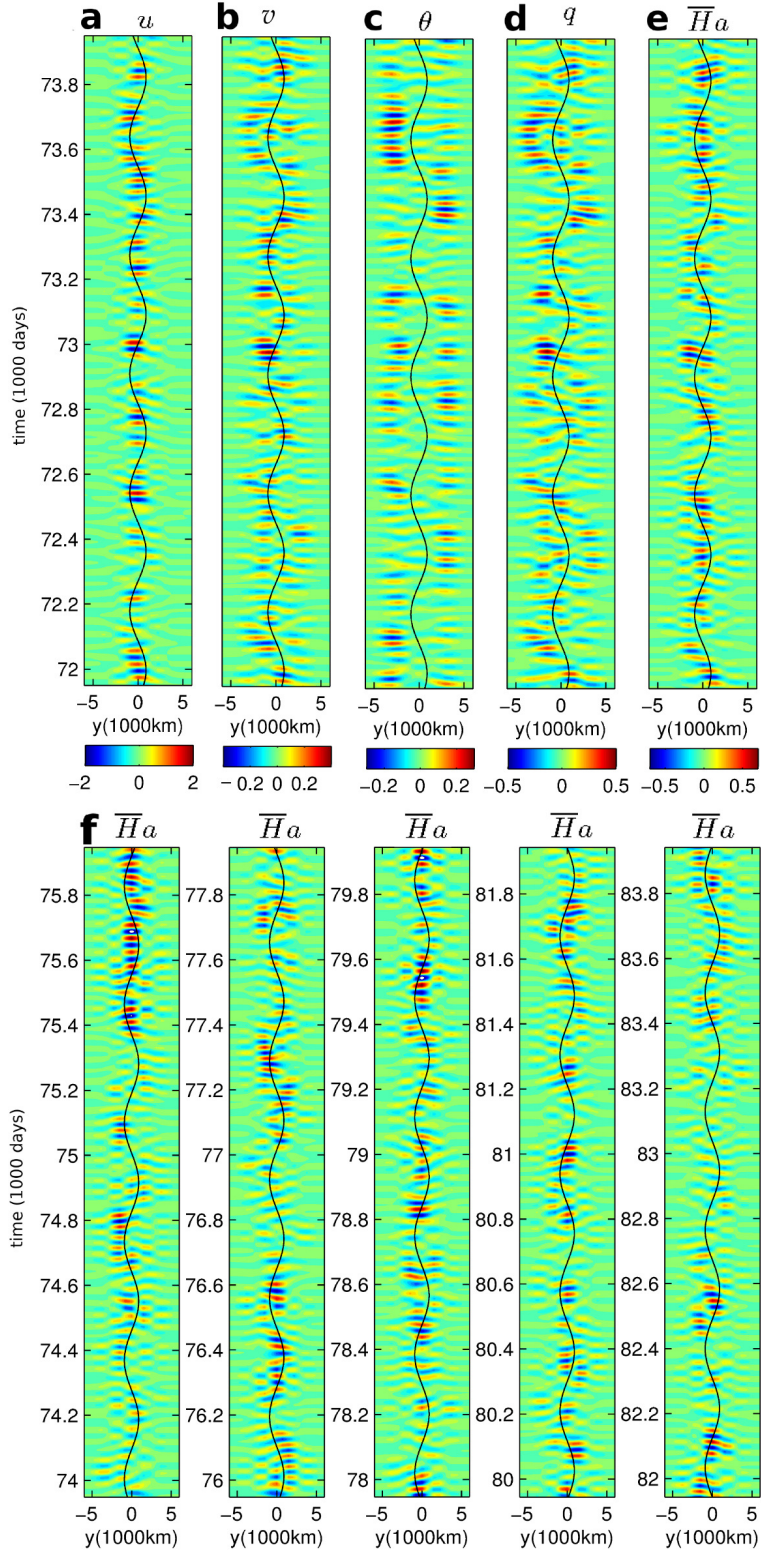


Figure 4: $y-t$ Hovmoller diagrams: for (a) u ($m.s^{-1}$), (b) v ($m.s^{-1}$), (c) θ (K), (d) q (K), and (e) \overline{Ha} ($K.day^{-1}$), as a function of meridional position location y (in 1000 km) and simulation time (in 1000 days). (f) repeats the Hovmoller diagram for \overline{Ha} at different times. The variables are filtered in the MJO band ($1 \leq k \leq 3$ and $1/90 \leq \omega \leq 1/30$ cpd), and considered at the warm pool zonal center ($x = 20,000$ km). The meridional position y_C of the warm pool center, varying with seasons, is overplotted (black line).

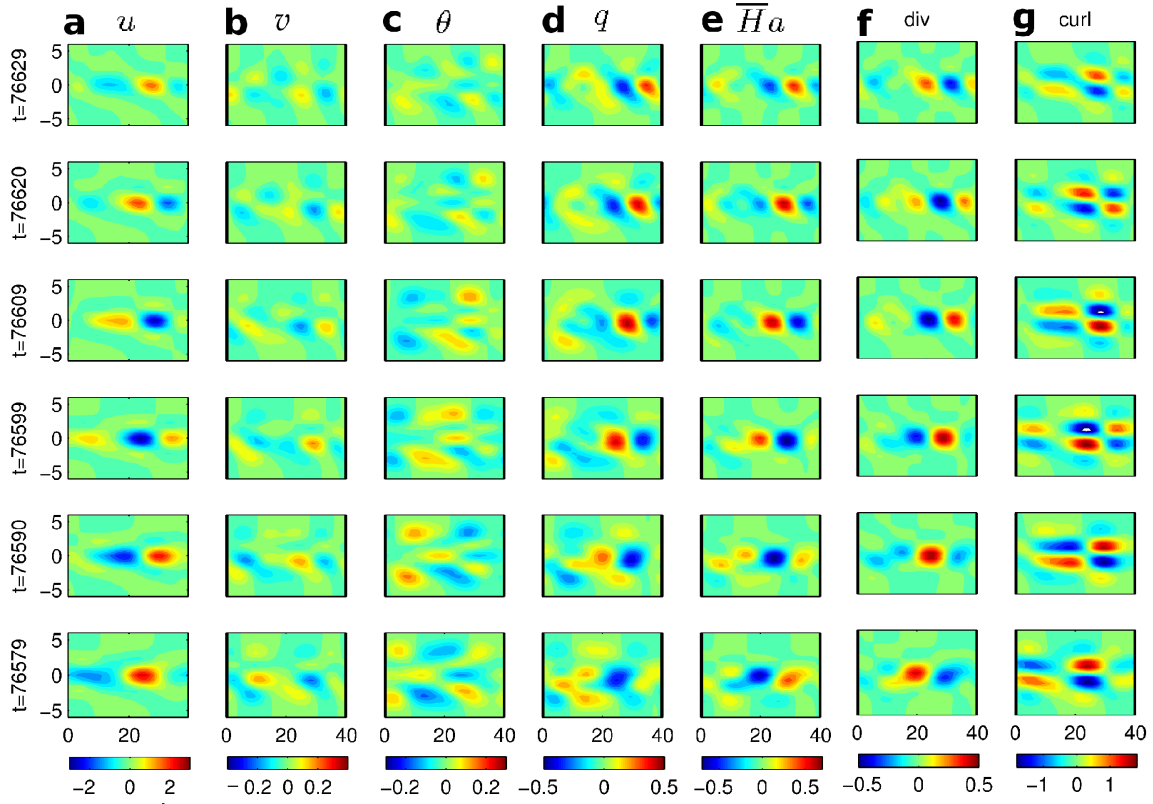


Figure 5: $x - y$ Snapshots for a symmetric intraseasonal event: for (a) u ($m.s^{-1}$), (b) v ($m.s^{-1}$), (c) θ (K), (d) q (K), (e) \overline{Ha} ($Kday^{-1}$), (f) divergence $\partial_x u + \partial_y v$ ($m.s^{-1})(1000km)^{-1}$, and (g) curl $\partial_x v - \partial_y u$ ($m.s^{-1})(1000km)^{-1}$, as a function of zonal position x (1000km) and meridional position y (1000km). Left label indicates simulation time for each snapshot (in days). The variables are filtered in the MJO band ($1 \leq k \leq 3$ and $1/90 \leq \omega \leq 1/30$ cpd).

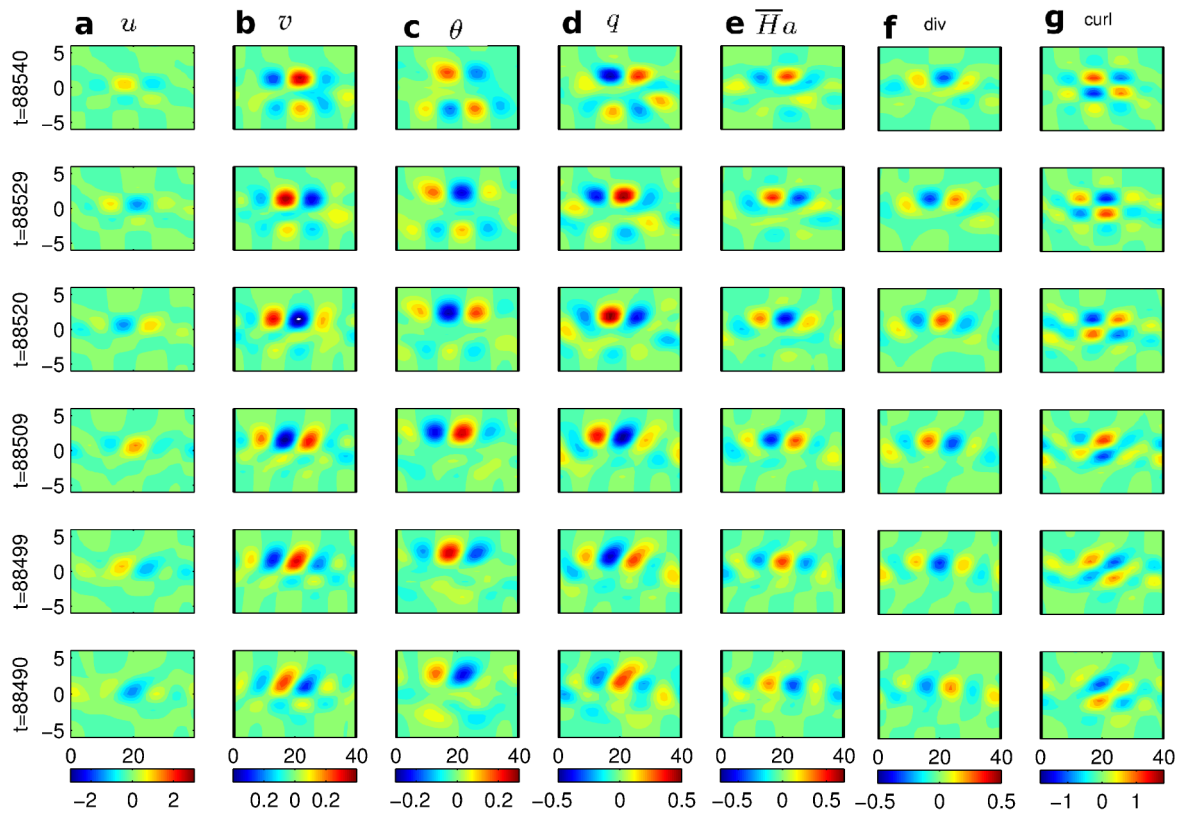


Figure 6: $x - y$ Snapshots for a half-quadrupole north (HQN) intraseasonal event (see legend of figure 5).

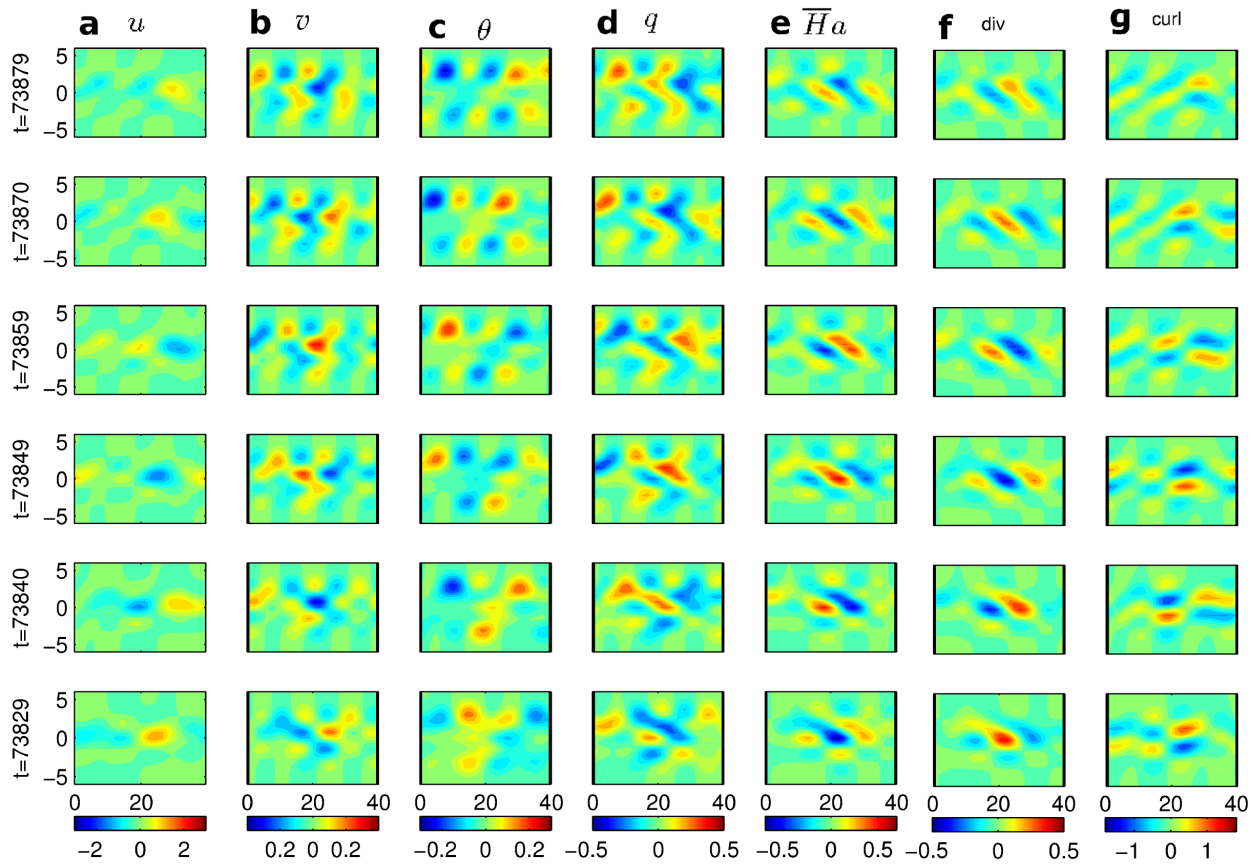


Figure 7: $x - y$ Snapshots for a tilted north (TN) intraseasonal event (see legend of figure 5).

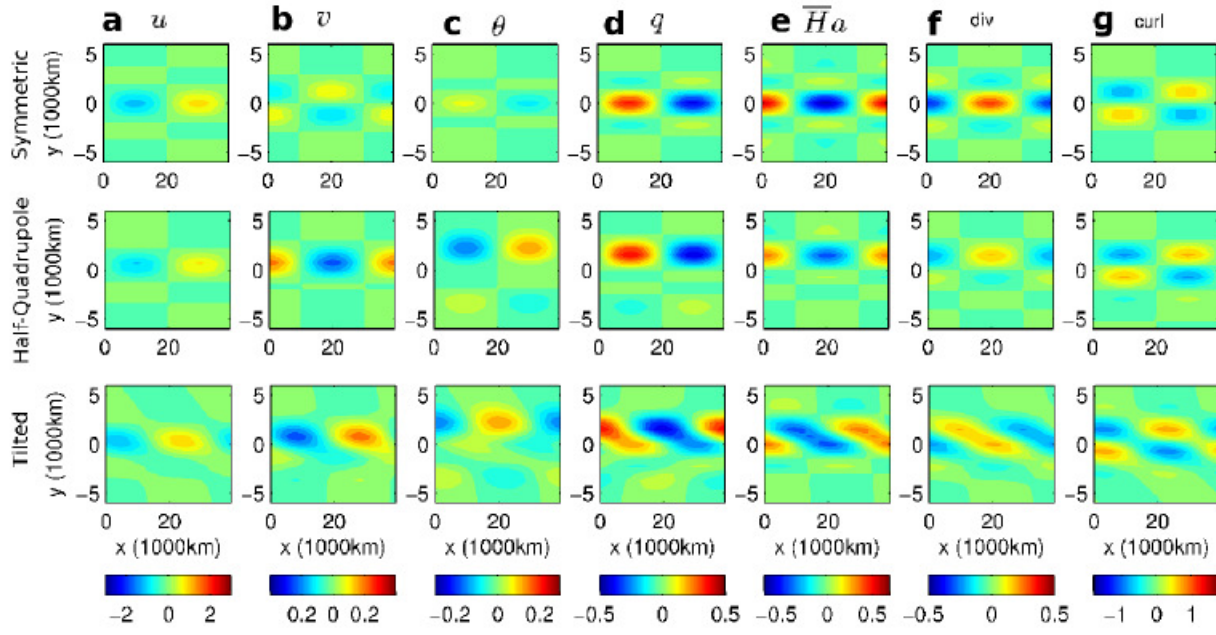


Figure 8: Atmospheric response to prescribed heating: for (a) u (ms^{-1}), (b) v (ms^{-1}), (c) θ (K), (d) q (K), (e) \overline{Ha} ($Kday^{-1}$), (f) divergence $\partial_x u + \partial_y v$ ($m.s^{-1})(1000km)^{-1}$, and (g) curl $\partial_x v - \partial_y u$ ($m.s^{-1})(1000km)^{-1}$, as a function of zonal position x (1000km) and meridional position y (1000km). This is shown for (top) a symmetric event, (middle) a half-quadrupole north (HQN) event, (bottom) a tilted north (TN) event. .

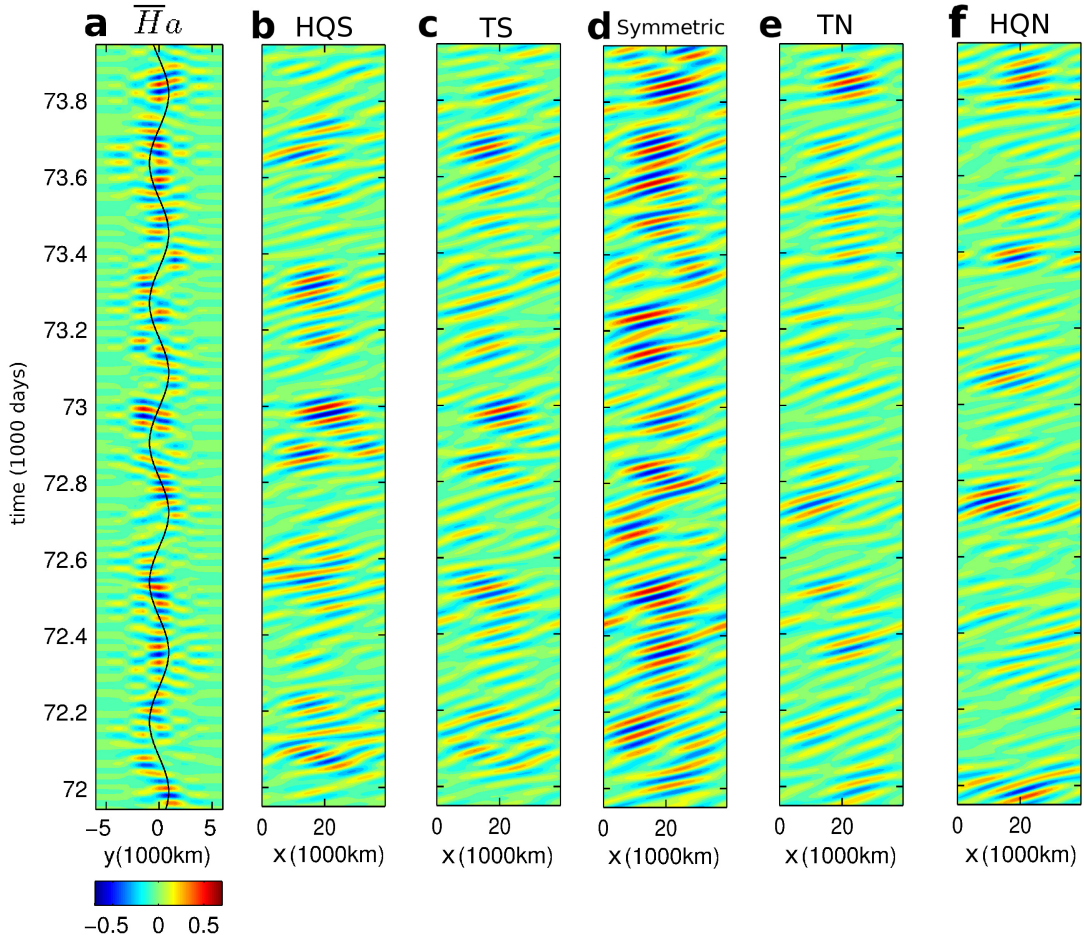


Figure 9: (a) $y - t$ Hovmoller diagram: for \overline{Ha} ($Kday^{-1}$), as a function of meridional position location y (in 1000 km) and simulation time (in 1000 days), considered at the warm pool zonal center ($x = 20,000 km$). (b-f): $x - t$ Hovmoller diagrams: for the index of (b) half-quadrupole south (HQS), (c) tilted south (TS), (d) symmetric, (e) tilted north (TN), and (f) half-quadrupole north (HQN) events, in $Kday^{-1}$ and as a function of zonal position location x (in 1000 km) and simulation time (1000 days).